

RADIATION SPECTRA FROM
ADVECTION-DOMINATED ACCRETION FLOWS
IN A GLOBAL MAGNETIC FIELD

MOTOKI KINO¹, OSAMU KABURAKI AND NAOHIRO YAMAZAKI

Astronomical Institute, Graduate School of Science, Tohoku University,
Aoba-ku, Sendai 980-8578, Japan;
kino@astr.tohoku.ac.jp, okabu@astr.tohoku.ac.jp, ietty@astr.tohoku.ac.jp

Draft version October 26, 2018

ABSTRACT

We calculate the radiation spectra from advection-dominated accretion flows (ADAFs), taking into account the effects of a global magnetic field. Calculation is based on the analytic model for magnetized ADAFs proposed by Kaburaki, where a large-scale magnetic field controls the accretion process. Adjusting a few parameters, we find that our model can well reproduce the observed spectrum of Sagittarius A*. The result is discussed in comparison with those of well-known ADAF models, where the turbulent viscosity controls the accretion process.

Subject headings: accretion, accretion disks—radiation mechanisms: non-thermal—Galaxy: center—magnetic fields

1. INTRODUCTION

The optically thin, advection-dominated accretion flows (ADAFs) have been studied by a number of authors during past several years (e.g. Narayan & Yi 1994, 1995a, b; Abramowicz et al. 1995; Nakamura et al. 1997, Manmoto, Mineshige & Kusunose 1997; Narayan et al. 1998). These models are very successful in describing both spectra and dynamics of accreting black hole systems such as those in binaries and in low-luminosity active galactic nuclei (AGNs). The observed spectra can be explained as follows. The radio emission is due to the synchrotron emission in turbulent magnetic fields in the accretion flow. These synchrotron photons serve as seed photons for the inverse Compton process by hot electrons. Once-scattered Compton photons are mainly distributed in the optical band and twice-scattered Compton photons, in soft X-ray band. Bremsstrahlung due to electron-electron and electron-proton collisions gives rise to the observed hard X-ray spectra.

Thus, these ADAF models provide a good framework for understanding the observed spectra. In these models, both angular momentum transfer and energy dissipation in the accretion flow is assumed to be undertaken by the turbulent viscosity whose size is specified by so-called α parameter. For this reason, hereafter we call this type of models the “viscous” ADAF model in this paper. The magnetic fields are regarded as of turbulence origin and are described by another parameter β which specifies the ratio of the magnetic pressure to the gas pressure.

However there is no reason to believe that the turbulent viscosity is the only candidate that controls the accretion processes. Rather, it is quite natural to think that some types of global magnetic fields may play an essential role. Indeed, there are some evidences for the presence of such an ordered magnetic field in the central region of our Galaxy (e.g., Yusef-Zadeh, Morris & Chance 1984).

As Kato, Fukue & Mineshige (1998) has pointed out the hydromagnetic turbulence in accretion disks may also generate global magnetic fields by dynamo processes due to the presence of helical motions. In view of such circumstances, another type of ADAF model has been proposed by one of the present authors (Kaburaki 1999, 2000; hereafter referred to as K99 and K00). In order to distinguish it from the above viscous ADAF models, hereafter we call it the “resistive” ADAF models since energy dissipation in the accretion flow is due to the electric resistivity and angular momentum transfer is supported not by the viscosity but by the magnetic stress of a large scale magnetic field.

The purpose of the present study is to calculate the expected radiation spectra from ADAFs in a global magnetic field based on the resistive ADAF model, in order to compare its predictions with those of the viscous ADAF models. As a most suitable candidate for such a comparison, Sgr A* is taken up here because it has been observed in many wave lengths as the nearest galactic nucleus and its spectrum has been reproduced many times by the successively advancing viscous ADAF models.

In §2, we introduce the set of analytic solutions for resistive ADAFs in a suitably scaled form and discuss their basic characteristics. The relevant radiation mechanisms and the methods of calculation of the fluxes are described in §3. These schemes are applied to Sgr A* in §4 and the results are discussed in comparison with those of the viscous ADAF models. Finally in §5, we summarize the main results and discuss some related issues.

2. RESISTIVE ADAF SOLUTION

As a basis of our calculation of spectra, we introduce here the set of analytic solutions constructing the resistive ADAF model. This set may be considered as a counter-

¹Present address: Department of Earth and Space Science, Graduate School of Science, Osaka University, Toyonaka, Osaka 560-0043, Japan
kino@vega.ess.sci.osaka-u.ac.jp

part of that found by Narayan & Yi (1994, 1995a) in the viscous ADAF scheme, but it should be emphasized that the former is not a self-similar solution as the latter. In the resistive ADAF model, there are three basic quantities and one parameter: mass of the central black hole M , mass accretion rate \dot{M} , strength of the external magnetic field $|B_0|$ and half-opening angle of the flow Δ , respectively. We introduce the following normalizations for these quantities and for the radial distance R :

$$m \equiv \frac{M}{10^6 M_\odot}, \quad \dot{m} \equiv \frac{\dot{M}}{\dot{M}_E}, \quad b_0 \equiv \frac{|B_0|}{1G}, \quad \delta \equiv \frac{\Delta}{0.1}, \quad r \equiv \frac{R}{R_{\text{out}}}, \quad (1)$$

where R_{out} denotes the radius of the disk's outer edge. The Eddington accretion rate is defined by $\dot{M}_E \equiv L_E/(0.1c^2)$, which includes the efficiency factor of 0.1. Note that this definition of \dot{M}_E and the normalization factor for black hole mass are different from those in K00. The latter is chosen here as $10^6 M_\odot$ for the convenience of the discussion of Sgr A*.

In spherical polar coordinates, the radius of outer edge and the radial-part functions of relevant physical quantities (for their angular parts, see also K99, K00) are written as

$$R_{\text{out}} = 1.5 \times 10^{16} b_0^{-4/5} \dot{m}^{2/5} m^{3/5} \text{ cm}, \quad (2)$$

$$|b_\varphi(r)| = 10 \delta^{-1} b_0 r^{-1} \text{ G}, \quad (3)$$

$$v_K(r) = 0.9 \times 10^8 b_0^{2/5} \dot{m}^{-1/5} m^{1/5} r^{-1/2} \text{ cm s}^{-1}, \quad (4)$$

$$P(r) = 4.0 \delta^{-2} b_0^2 r^{-2} \text{ dyne cm}^{-2}, \quad (5)$$

$$T(r) = 1.8 \times 10^7 b_0^{4/5} \dot{m}^{-2/5} m^{2/5} r^{-1} \text{ K}, \quad (6)$$

$$\rho(r) = 1.3 \times 10^{-15} \delta^{-2} b_0^{6/5} \dot{m}^{2/5} m^{-2/5} r^{-1} \text{ g cm}^{-3}, \quad (7)$$

where b_φ is the toroidal magnetic field, v_K is the Kepler velocity, P is the gas pressure, T is the temperature (common to electrons and ions) and ρ is the density. Owing to the non-negligible pressure term in the radial force balance, the toroidal velocity in the disk is reduced by a factor of $1/\sqrt{3}$ from the Kepler value. The surface density and the optical depth are given, respectively, by

$$\Sigma(r) = \Sigma = 4.1 \delta^{-1} b_0^{2/5} \dot{m}^{4/5} m^{1/5} \text{ g cm}^{-2}, \quad (8)$$

$$\tau_{\text{es}}(r) \simeq \frac{1}{2} \kappa_{\text{es}} \Sigma = 8.2 \times 10^{-1} \delta^{-1} b_0^{2/5} \dot{m}^{4/5} m^{1/5}, \quad (9)$$

where κ_{es} is the opacity for electron scattering. Note that these are independent of r in the present model.

Fig. 1 shows a schematic picture of an accretion disk in a global magnetic field, whose precise structure is described by the solution given above. Otherwise uniform external magnetic field is twisted by the rotational motion of accreting plasma, and there develops a large toroidal magnetic field in the middle latitude region. The behavior of this component, especially within the geometrically thin accretion flow, is given as $-b_\varphi \tanh \xi$ in the resistive ADAF solution, where $\xi = (\theta - \pi/2)/\Delta$ is the normalized angular variable. Owing to the appearance of a global b_φ , angular momentum of the accreting plasma becomes able to be carried away by the magnetic stress to distant regions along the poloidal magnetic field. The extraction of angular momentum guarantees the inward motion of the plasma, which gradually becomes large until it reaches near the rotational velocity at around the inner edge of the accretion disk. Although the magnetic lines of force are

also bent inwardly toward the center of gravitational attraction, it has been shown that the dominant component is the toroidal one. This component also plays an essential role in the plasma confinement toward the equatorial plane and keeps it geometrically thin through its magnetic pressure.

Before going into the detailed discussion of the radiative processes, we briefly mention some similarities and differences in the basic features of the viscous and resistive ADAF models. It is worth noting that, in spite of the essential difference in the mechanisms of angular momentum transport and energy dissipation, the predictions for quantities such as temperature, density and optical depth are quite similar in both models. The temperatures in both models are as high as a fraction of the virial temperature of ions. Indeed, this is the case in the viscous models, though the electron temperature may deviates from it in the inner regions (e.g., Narayan & Yi 1995b), and so also in the resistive model as can be confirmed from the analytic expression of T (K99, K00). Such a high temperature makes a sharp contrast with the case of standard α -disks (e.g., Frank, King & Raine 1992). Further, for a sub-Eddington mass accretion rate, the optical depth is dominated by the electron scattering and is smaller than unity. These are therefore common features of sub-Eddington ADAF models as expected.

As one of the main differences, it may be stressed that the magnetic field in the resistive ADAF model is an ordered magnetic field and is determined self-consistently in the model from a boundary value. Therefore, the strength of the field is not a parameter as in the viscous ADAF models. The ordered magnetic field extract angular momentum from the accreting plasma and confines it in a disk structure against the gas pressure. Gravitational energy is released in the disk as the Joule heating and also as compressional heating of the flow. In the above analytic model of resistive ADAFs, these energies are fully advected down the stream. We calculate the radiation from the disk as a small perturbation from this solution.

Another distinction may be in the energy partition between the electron and ion components. The viscous ADAF models assume that the viscous dissipation, which is large at large radii, heats mainly ions. Since the efficiency of radiation cooling is very small for ions compared with electrons and since energy transfer to the electron component is estimated to be negligible (Manmoto et al. 1997) except in outer portions, the flow is fully advective in most portions. For the electron component, on the other hand, the radiative cooling is balanced by the advective heating, near the inner edge. The electron temperature, therefore, deviates downwards largely from the ion temperature thus realizing a two-temperature structure.

In contrast to the viscous heating, the resistive dissipation becomes large at small radii and seems to preferentially heat the electron component as suggested by Bisnovaty-Kogan & Lovelace (1997). In this case, the temperature difference is expected to remain rather small because the heating is effective for effective radiator. In any case, the resistive ADAF model in its present version assume a common temperature to both components, for simplicity. The examination of its two-temperature version may belong to a future work.

3. CALCULATION OF SPECTRUM

As mentioned above, the radiation spectrum from a resistive ADAF is calculated based on the analytic solution introduced in the previous section. Back reactions of the radiation cooling to this fully advective solution are negligible as far as its fraction in the total cooling rate is small.

This has been roughly checked in a previous paper (K00). The method of calculating radiation fluxes described in this section will be applied to Sgr A* in the next section. The observed spectrum of Sgr A* in the frequency range from radio up to X-ray range is successfully explained in the viscous ADAF models by the three processes, i.e., synchrotron radiation, bremsstrahlung and inverse Compton scattering (Narayan, Yi & Mahadevan 1995; Manmoto et al. 1997; Narayan et al. 1998). Although there may be some other components such as the radio-frequency excess over the Rayleigh-Jeans spectrum and γ -ray peak both of which need separate explanations (see, e.g., Mahadevan 1999 for the former, and Mahadevan, Narayan & Krolik 1997 for the latter), we ignore these components here for simplicity.

Among the above three processes, the Compton scattering is treated separately from the other processes of emission and absorption. Therefore, we divide the total flux into two parts: the flux due to bremsstrahlung and synchrotron process F_ν and that due to the inverse Compton process F'_ν . The obtained fluxes are both integrated over the entire surfaces (upper and lower ones) of a disk, and added up to obtain the luminosity per unit frequency L_ν .

Temperature in the flow is vertically isothermal in the present model. In calculating the emission and absorption processes, the flow is further assumed to be locally plane parallel. Solving the radiative diffusion equation at a given radius R , we obtain the flux of the unscattered photons F_ν emanating from one side of the disk (Rybicki & Lightman 1979) as

$$F_\nu = \frac{2\pi}{\sqrt{3}} B_\nu \left[1 - \exp(-2\sqrt{3}\tau_\nu^*) \right], \quad (10)$$

where B_ν is the Planck intensity and τ_ν^* is the vertical optical depth for absorption,

$$\tau_\nu^*(R) \simeq \frac{\sqrt{\pi}}{2} \kappa_\nu R \Delta. \quad (11)$$

Assuming the local thermodynamic equilibrium (LTE), we can express the absorption coefficient κ_ν at the equatorial plane in terms of the volume emissivities χ_ν 's for bremsstrahlung and synchrotron processes:

$$\kappa_\nu = \frac{\chi_{\nu,\text{br}} + \chi_{\nu,\text{sy}}}{4\pi B_\nu}. \quad (12)$$

Thus, equation (10) includes not only the effect of free-free absorption but also of synchrotron self-absorption at low frequencies.

As the distribution function for thermal electrons, we assume that of the relativistic Maxwellian (in its normalized form),

$$N_e(\gamma) d\gamma = \frac{\gamma^2 \beta \exp(-\frac{\gamma}{\theta_e})}{\theta_e K_2(\frac{1}{\theta_e})} d\gamma, \quad \theta_e = \frac{k_B T_e}{m_e c^2}, \quad (13)$$

because ADAFs tend to have so high temperatures that electron thermal energy can exceed its rest mass energy. Here, γ is the Lorentz factor, k_B is the Boltzmann constant and K_2 is the 2nd modified Bessel function. Actually, we use this formula only in the calculation of Comptonized photon flux below, while in those of bremsstrahlung and synchrotron processes we follow the works of Narayan & Yi (1995b), and Manmoto et al. (1997) where it is replaced by a numerical fitting function.

3.1. Bremsstrahlung

At relativistic temperatures, we must take into account not only electron-proton but also electron-electron encounters. Therefore, the total bremsstrahlung cooling rate per unit volume is written as

$$q_{\text{br}}^- = q_{ei}^- + q_{ee}^-, \quad (14)$$

where the subscripts ei and ee denote the electron-ion and electron-electron processes, respectively. The explicit expressions of the cooling rates are as follows. For the electron-proton process,

$$\begin{aligned} q_{ei}^- &= 1.25 n_e^2 \sigma_T \alpha_f m_e c^2 F_{ei}(\theta_e) \\ &= 1.48 \times 10^{-22} n_e^2 F_{ei}(\theta_e) \text{ ergs cm}^{-3} \text{ s}^{-1}, \end{aligned} \quad (15)$$

where n_e is the electron number density, α_f is the fine-structure constant and σ_T is the Thomson cross-section, and further

$$\begin{aligned} F_{ei}(\theta_e) &= 4 \left(\frac{2\theta_e}{\pi^3} \right)^{0.5} (1 + 1.781\theta_e^{1.34}) \quad \text{for } \theta_e < 1, \\ &= \frac{9\theta_e}{2\pi} [\ln(1.123\theta_e + 0.48) + 1.5] \\ &\quad \text{for } \theta_e > 1. \end{aligned} \quad (16)$$

For the electron-electron process,

$$\begin{aligned} q_{ee}^- &= n_e^2 c r_e^2 m_e c^2 \alpha_f \frac{20}{9\pi^{0.5}} (44 - 3\pi^2) \theta_e^{3/2} \\ &\quad \times (1 + 1.1\theta_e + \theta_e^2 - 1.25\theta_e^{5/2}) \\ &= 2.56 \times 10^{-22} n_e^2 \theta_e^{3/2} (1 + 1.1\theta_e + \theta_e^2 - 1.25\theta_e^{5/2}) \\ &\quad \text{ergs cm}^{-3} \text{ s}^{-1} \end{aligned} \quad (17)$$

when $\theta_e < 1$, and

$$\begin{aligned} q_{ee}^- &= n_e^2 c r_e^2 m_e c^2 \alpha_f 24\theta_e (\ln 2\eta\theta_e + 1.28) \\ &= 3.40 \times 10^{-22} n_e^2 \theta_e (\ln 1.123\theta_e + 1.28) \\ &\quad \text{ergs cm}^{-3} \text{ s}^{-1} \end{aligned} \quad (18)$$

when $\theta_e > 1$. Here, $r_e = e^2/m_e c^2$ is the classical electron radius and $\eta = \exp(-\gamma_E) = 0.5616$.

The emissivity per frequency is given by

$$\chi_{\nu,\text{br}} = q_{\text{br}}^- \bar{G} \exp\left(-\frac{h\nu}{k_B T_e}\right) \text{ ergs cm}^{-3} \text{ s}^{-1} \text{ Hz}^{-1}, \quad (19)$$

where h is the Planck constant and \bar{G} is the Gaunt factor which is written (Rybicki & Lightman 1979) as

$$\begin{aligned} \bar{G} &= \frac{h}{k_B T_e} \left(\frac{3 k_B T_e}{\pi h\nu} \right)^{1/2} \quad \text{for } \frac{h\nu}{k_B T_e} > 1, \\ &= \frac{h}{k_B T_e} \frac{\sqrt{3}}{\pi} \ln \left(\frac{4 k_B T_e}{\zeta h\nu} \right) \quad \text{for } \frac{h\nu}{k_B T_e} < 1. \end{aligned} \quad (20)$$

The above cited formulæ contain a few minor defects. For example, the non-relativistic limit calculated for electron-ion process from equations (16) and (20) differs by about 35% from the standard formula (Rybicki & Lightman 1979). Equation (20) assumes the same values of the Gaunt factor for both electron-electron and electron-ion processes. In spite of these defects, we adopt the above

formule according to Narayan & Yi (1995b) and Manmoto et al. (1997), considering that these are the best ones we can employ at present throughout the energy range of our interest. The adoption of the same formule as in the previous calculations is also suitable for the purpose of comparison of the predictions of different models, such as the viscous and resistive ones.

3.2. Synchrotron Emission

Synchrotron emission is an essential process to produce the radio wave-length part of the spectra from optically thin ADAFs in AGNs. Especially in the resistive ADAF model, some information about the strength of the ambient magnetic field may be obtained from the process of spectral fitting.

The optically-thin synchrotron emissivity by relativistic Maxwellian electrons is calculated from the formula (Narayan & Yi 1995b; Mahadevan, Narayan & Yi 1996),

$$\chi_{\nu, \text{sy}} = 4.43 \times 10^{-30} \frac{4\pi n_e \nu}{K_2(1/\theta_e)} I' \left(\frac{4\pi m_e c \nu}{3eB\theta_e^2} \right) \text{ ergs cm}^{-3} \text{ s}^{-1} \text{ Hz}^{-1}, \quad (21)$$

where e is the elementary charge and

$$I'(x) = \frac{4.0505}{x^{1/6}} \left(1 + \frac{0.4}{x^{1/4}} + \frac{0.5316}{x^{1/2}} \right) \exp(-1.8899x^{1/3}) \quad (22)$$

In equation(21), the argument of I' is specified as

$$x \equiv \frac{2\nu}{3\nu_0\theta_e^2}, \quad \nu_0 \equiv \frac{e|B|}{2\pi m_e c}, \quad (23)$$

where B is the local value of magnetic field for which we substitute b_φ .

3.3. Inverse Compton Scattering

The soft photons whose flux is given by equation (10) are Compton scattered by the relativistic electrons in the flow. We adopt the rate equation of Coppi & Blandford (1990) as the basis of our considerations. This equation applies to homogeneous, isotropic distributions. The first term on the right-hand side of their equation describes the rate of decrease in the photon's number density with a given energy owing to the scattering into other energies, while the second term does the increase owing to the scattering into this energy from other energies.

In the situations of our interest, we can neglect the first term because the number density of Comptonized photons are small compared with that of the seed photons. Instead, we use the second term iteratively to calculate the effects of multiple scattering. The scattering occurs on the average when the condition $c\sigma_T n_e dt = 1$ is satisfied, where t is time and n_e is the number density of electrons. The probability that such a condition is satisfied j -times before the photons come out of the surface may be given by the Poisson formula,

$$p_j = \frac{\tau_e^j e^{-\tau_e}}{j!}. \quad (24)$$

Then, the production rate for the photons with a normalized energy $\epsilon \equiv h\nu/m_e c^2$ is given by

$$\frac{dn(\epsilon)}{c\sigma_T n_e dt} = \sum_{j=1}^{\infty} p_j \int d\gamma_j \dots d\gamma_1 N_e(\gamma_j) \dots N_e(\gamma_1)$$

$$\begin{aligned} & \times \int d\epsilon_j \dots d\epsilon_1 \\ & \left[P(\epsilon; \epsilon_j, \gamma_j) \dots P(\epsilon_2; \epsilon_1, \gamma_1) R(\epsilon_j, \gamma_j) \dots \right. \\ & \left. R(\epsilon_1, \gamma_1) n_{\text{in}}(\epsilon_1) \right], \end{aligned} \quad (25)$$

where m_e is the electron mass and n_{in} is the number density of seed photons.

The non-dimensional scattering rate $R(\epsilon, \gamma)$ including Klein-Nishina cross section σ_{KN} is written explicitly (Coppi & Blandford 1990) as

$$\begin{aligned} R(\epsilon, \gamma) &= \int_{-1}^1 \frac{d\mu}{2} (1 - \beta\mu) \frac{\sigma_{\text{KN}}(\beta, \epsilon, \mu)}{\sigma_T} \\ &= \frac{3}{32\gamma^2\beta\epsilon^2} \int_{2\gamma(1-\beta)\epsilon}^{2\gamma(1+\beta)\epsilon} dx \left[\left(1 - \frac{4}{x} - \frac{8}{x^2} \right) \ln(1+x) \right. \\ & \quad \left. + \frac{1}{2} + \frac{8}{x} - \frac{1}{2(1+x)^2} \right] \text{ cm}^3 \text{ s}^{-1}. \end{aligned} \quad (26)$$

Scattered-photon distribution is denoted by $P(\epsilon; \epsilon', \gamma)$ and, in the present calculation, approximated by a δ -function (Lightman & Zdziarski 1987, Fabian et al. 1986):

$$P(\epsilon; \epsilon', \gamma) = \delta \left(\epsilon - \frac{4\gamma^2}{3} \epsilon' \right). \quad (27)$$

This is merely for simplicity and a more exact expression has been derived by Jones (1968) and corrected afterwards by Coppi & Blandford (1990).

Although the sum in equation (25) runs to infinity, it seems appropriate to assume that photons which are scattered more than certain times become saturated and obey the Wien distribution $\propto \nu^3 \exp(-h\nu/kT_e)$ (e.g., Manmoto et al. 1997). In view of the smallness of the optical depth in most sub-Eddington ADAFs ($\tau_{\text{es}} < 10^{-3}$, in the case of Sgr A*), however, we truncate the power series in τ_{es} at $j = 2$ and ignore the saturation effect. After performing the integrations containing δ -functions and transforming the photon number densities into fluxes by multiplying $ch\epsilon/2$ on both sides of equation (25), we obtain

$$F'_\nu(0) = e^{-\tau_{\text{es}}} \left[\tau_{\text{es}} F_\nu^{(1)} + \frac{\tau_{\text{es}}^2}{2} F_\nu^{(2)} \right], \quad (28)$$

where once- and twice-scattered fluxes are given, respectively, by

$$F_\nu^{(1)} \equiv \int_1^\infty d\gamma_1 N_e(\gamma_1) R \left(\frac{3\epsilon}{4\gamma_1^2}, \gamma_1 \right) F_{\text{in}} \left(\frac{3\epsilon}{4\gamma_1^2} \right), \quad (29)$$

$$\begin{aligned} F_\nu^{(2)} &\equiv \int_1^\infty d\gamma_2 \int_1^\infty d\gamma_1 N_e(\gamma_2) N_e(\gamma_1) \\ & \times R \left(\frac{3\epsilon}{4\gamma_2^2}, \gamma_2 \right) R \left(\frac{3}{4\gamma_2^2} \frac{3\epsilon}{4\gamma_1^2}, \gamma_1 \right) \\ & \times F_{\text{in}} \left(\frac{3}{4\gamma_2^2} \frac{3\epsilon}{4\gamma_1^2} \right) \end{aligned} \quad (30)$$

with the definition $F_{\nu, \text{in}} = (ch\epsilon/2)n_{\text{in}}(\epsilon) \equiv F_{\text{in}}(\epsilon)$. As the incident flux $F_{\nu, \text{in}}$ in the above expressions, the result from equation (10) should be used. The effects of low energy tail ($\beta < 1$) in the electron distribution is neglected in performing the γ -integrals.

4. APPLICATION TO SAGITTARIUS A*

In order to compare the resistive ADAF model with the current models of viscous ADAFs in their predictions of spectra from accretion flows, we apply the former model to Sgr A*. The observed spectral data available so far have been compiled by Narayan et al. (1998). They assume that the interstellar column density is $N_{\text{H}} = 6 \times 10^{22} \text{ cm}^{-2}$ and the distance to the Galactic center is $d = 8.5 \text{ kpc}$. In judging the accuracy of fittings between the calculated and observed spectra, a considerable weight has been put on the high resolution data points such as the VLBI radio (86 GHz) data and the *ROSAT* X-ray data. It should be kept in mind, however, that the *ROSAT* data may be interpreted as an upper limit because its resolution (PSPC) $\sim 20''$ is not considered as satisfactory and that other issues like the value of N_{H} are still under discussion.

We discuss the two cases in the resistive model, which will be called the compact-disk and the extended-disk models, respectively. These names come from the difference in extension of the disk which is represented by the radius ratio of the inner to the outer edges, $R_{\text{in}}/R_{\text{out}} = r_{\text{in}}$. As confirmed below, this value is largely affected by the choice of position of the inner edge, R_{in} .

4.1. Compact Disk Model

According to the spirit of original resistive ADAF model, the inner edge in this case is determined by the magnetic flux conservation (K00). This gives an expression

$$R_{\text{in}} = (1 + \Delta^{-1})^{-2} R_{\text{out}} \simeq \Delta^2 R_{\text{out}}, \quad (31)$$

where the last expression is valid only for thin disks ($\Delta \ll 1$). Note that this procedure is independent of the notion of the marginally stable orbit around black holes. The outer edge has been fixed, on the other hand, from the mass conservation as

$$R_{\text{out}} = \left(\frac{3GM\dot{M}^2}{B_0^4} \right)^{1/5}. \quad (32)$$

Fig. 2 shows the best fit spectrum in this model and the set of best fit parameters is

$$\begin{aligned} M &= 3.9 \times 10^5 M_{\odot}, \\ \dot{M} &= 1.2 \times 10^{-4} \dot{M}_{\text{E}} = 1.0 \times 10^{-6} M_{\odot} \text{ yr}^{-1}, \\ |B_0| &= 0.7 \text{ G}, \quad \Delta = 0.14 \text{ rad}. \end{aligned} \quad (33)$$

From these values, other quantities of our interest are fixed as follows:

$$\begin{aligned} R_{\text{in}} &= 6.1 \times 10^{12} \text{ cm}, & R_{\text{out}} &= 3.1 \times 10^{14} \text{ cm}, \\ T &= 3.4 \times 10^8 r^{-1} \text{ K}, & |b_{\varphi}| &= 5.0 r^{-1} \text{ G}, \\ \rho &= 1.8 \times 10^{-17} r^{-1} \text{ g cm}^{-3}, \\ \tau_{\text{es}} &= 3.1 \times 10^{-4}. \end{aligned} \quad (34)$$

Thus, it turns out that the inner edge of the present model is fairly large compared with the marginally stable orbit, $R_{\text{ms}} = 3.5 \times 10^{11} \text{ cm}$, for a Schwarzschild hole of the above mass.

The changes in the spectrum caused by varying central mass M , accretion rate \dot{M} , external magnetic field $|B_0|$ and disk's half-opening angle Δ are demonstrated in Figs. 3, 4, 5 and 6, respectively. The spectral features are anyway quite analogous to those predicted by the viscous ADAF models. The results of a detailed comparison between the resistive and viscous ADAF models will be discussed in the final subsection, based on the predicted spectral features.

4.2. Extended Disk Model

In this model, the inner edge of the accretion disk is set at the radius of the marginally stable circular orbit around a Schwarzschild black hole,

$$R_{\text{in}} = R_{\text{ms}} = 3R_{\text{G}} = \frac{6GM}{c^2}, \quad (35)$$

where R_{G} is the gravitational radius of the hole. This choice is motivated by the expectation that at around this radius the infall velocity inevitably becomes of the order of the rotational velocity, (i.e., $\mathfrak{R} \sim 1$ where \mathfrak{R} is the magnetic Reynolds number, see K99, K00). The definition of the outer edge is the same as in the compact disk model. Note that the above definition of the inner edge is adopted also in the viscous ADAF models.

The best fit parameters in this model are

$$\begin{aligned} M &= 1.0 \times 10^6 M_{\odot}, \\ \dot{M} &= 1.3 \times 10^{-4} \dot{M}_{\text{E}} = 2.9 \times 10^{-6} M_{\odot} \text{ yr}^{-1}, \\ |B_0| &= 1.0 \times 10^{-6} \text{ G}, \quad \Delta = 0.20 \text{ rad}. \end{aligned} \quad (36)$$

These are used to fix the values of various scaled quantities:

$$\begin{aligned} R_{\text{in}} &= 8.9 \times 10^{11} \text{ cm}, & R_{\text{out}} &= 2.7 \times 10^{19} \text{ cm}, \\ T &= 1.0 \times 10^4 r^{-1} \text{ K}, & |b_{\varphi}| &= 5.0 \times 10^{-6} r^{-1} \text{ G}, \\ \rho &= 5.9 \times 10^{-25} r^{-1} \text{ g cm}^{-3}, \\ \tau_{\text{es}} &= 1.3 \times 10^{-6}. \end{aligned} \quad (37)$$

The best fit curve is shown in Fig. 7. The changes in the spectrum caused by varying central mass M , accretion rate \dot{M} , external magnetic field $|B_0|$ and disk's half-opening angle Δ are demonstrated in Figs. 8, 9, 10 and 11, respectively. The spectral shapes are very different from those of the compact-disk case and of the viscous ADAF models. Synchrotron emission has a very wide peak and bremsstrahlung is negligibly small. The former fact is due to a high temperature at the inner edge (see sub-subsection 4.3.2) and the latter, to lower densities in the disk. The emission in the X-ray band is supported by the inverse Compton scattering from the radio band. The temperature near the outer edge falls even to such a small value that the assumption of complete ionization becomes invalid. Although the position of outer edge may seem to be irrelevant from a viewpoint of spectrum, it is nevertheless important also in this case as a fitting boundary of the inner magnetic field to the external one. The fitting predicts that the boundary value is comparable to the interstellar field (a few μG).

The fitting both to 86 GHz and *ROSAT* X-ray data points is possible also in this model. However, it is clear that the fitting curve runs above the observed upper limits in the IR band. The fitting in the frequency range from 100 to 1000 GHz also becomes considerably poor compared with the case of compact disk. For these reasons, we judge that this model cannot reproduce the observed broadband spectrum of Sgr A*. This fact suggests again that the inner edge of the accretion disk does not coincide with the marginally stable orbit. The wide range of the disk's radii which is obtained from this fitting implies that $\mathfrak{R}(R_{\text{out}}) \sim 6 \times 10^3$. Since $\mathfrak{R}(R)$ represents the ratio of toroidal to poloidal magnetic fields, most parts of the disk are very likely to be unstable to global MHD instabilities of helical type. For this reason too, we consider that the present case (i.e., $R_{\text{in}} = R_{\text{ms}}$) is quite unrealistic, at least, for Sgr A*.

4.3. Viscous v.s. Resistive ADAFs

4.3.1. Dependence on Black Hole Mass

The spectra calculated from ADAF models of both viscous and resistive types commonly have the saturated part at the lower ends of the spectra due to the synchrotron self-absorption. It is of great interest to see that the luminosity νL_ν of this part is essential to determine the mass of the central black hole, in both types of models. Especially, in the viscous model, the luminosity of this frequency part is determined almost only by the black hole mass. The reason is as follows.

The temperature in ADAFs may be considered essentially as the ion virial temperature and hence decreases as $\sim R^{-1}$. Apart from a numerical factor due to a reduced Keplerian rotation, this is exactly true in the resistive model. This is also true in the viscous models for the main part of an accretion flow except in the inner region where the electron temperature deviates from the ion temperature and remains almost constant (e.g., Narayan & Yi 1995b). Therefore, the contribution to the spectrum from each annulus of radius R and width dR is equal. Integrating these contributions up to the outer edge, we obtain $L_\nu^{\text{RJ}} \propto T_e(R_{\text{in}})R_{\text{in}}R_{\text{out}} = T_e(R_{\text{out}})R_{\text{out}}^2$, where R_{in} is the radius of the disk's inner edge in the resistive model and of the outer edge of the two-temperature region in the viscous models.

We have $T_e R \propto m$ commonly to both types of ADAF models. Further, since radius scales as the gravitational radius in the case of viscous ADAFs, we obtain the mass dependence

$$L_\nu^{\text{RJ}} \propto m^2 \quad (\text{viscous ADAF}), \quad (38)$$

confirming the above statement. On the other hand, in the case of resistive ADAFs, we have

$$L_\nu^{\text{RJ}} \propto b_0^{-4/5} \dot{m}^{2/5} m^{8/5} \quad (\text{resistive ADAF}), \quad (39)$$

where the dependences on the parameters other than m have come from the expression of R_{out} . In spite of these dependences, the mass dependence is essential also in this case. This is because the dependence on \dot{m} is rather weak and the value of b_0 is strongly restricted from the position of the synchrotron peak (see the discussion below).

4.3.2. Synchrotron Peak

We estimate the synchrotron peak frequency following Mahadevan (1997), and examine its behavior in both viscous and resistive models. For each annulus of radius R and width dR , the synchrotron photons in the radio range up to a critical frequency ν_c are strongly self-absorbed and result in the Rayleigh-Jeans spectrum. Therefore, the critical frequency of the spectrum is determined by equating the contributions to L_ν from optically thick and thin sides of the frequency:

$$\begin{aligned} & 2\pi \frac{\nu_c^2}{c^2} k_B T_e(R) 2\pi R dR \\ &= 4.43 \times 10^{-30} \frac{4\pi n_e \nu_c}{K_2(1/\theta_e)} I'(x_c) 4\pi \Delta R^2 dR, \end{aligned} \quad (40)$$

where x_c is defined as $x_c = 2\nu_c/(3\nu_0\theta_e^2)$. Solving this equation, we can determine the value of x_c numerically (Appendix B of Mahadevan 1997). Provided that this value does not depend strongly on R , Δ and other parameters, we obtain

$$\nu_c = \frac{3}{2} \theta_e^2 \nu_0 x_c \propto T_e^2(r) B(r). \quad (41)$$

If the disk has uniform temperature and magnetic field, then the synchrotron peak is rather sharp and has a well-defined peak frequency at ν_c .

When they vary with the radius R , however, substitution of the r -dependences of T_e and B in both viscous and resistive ADAF models yield

$$\begin{aligned} \nu_c &\propto \alpha^{-1/2} (1-\beta)^{1/2} \dot{m}^{1/2} m^{-1/2} r^{-13/4} \\ &\quad (\text{viscous ADAF}), \\ &\propto \delta^{-1} b_0^{13/5} \dot{m}^{-4/5} m^{4/5} r^{-3} \\ &\quad (\text{resistive ADAF}). \end{aligned} \quad (42)$$

This means that ν_c is larger for smaller radii and the higher most cutoff is due to the inner edge. The position of peak of the superposed emission is then given as $\nu_p = \nu_c(r_p)$, where r_p is the radius whose contribution to the synchrotron emission is most dominant. The fairly narrow peak obtained in the compact-disk case indicates that r_p is located near the inner edge and the global peak shape is determined mainly by the inner most region of the disk.

On the contrary, the synchrotron peak becomes very broad and dull in the extended-disk case. We have confirmed that the low-frequency side of the broad peak is due to a superposition of the contributions from annuli of $R_{\text{ms}} \sim 10R_{\text{ms}}$. However, the dull shape on the high-frequency side of the peak may be mainly due to a resulting high temperature ($T \sim 3 \times 10^{10}$ K) at the smaller inner edge. Actually, owing to this high temperature and low densities near the inner edge, the synchrotron self-absorption becomes less important in the high-frequency radio band and the intrinsic shape of the synchrotron emission at the mildly relativistic temperature (Mahadevan et al. 1996) can appear on the high-frequency side.

In any case, since r_p is a numerical factor, we can speak of the parameter dependences of the peak frequency ν_p based on equation (42). Note that the dependences on m and \dot{m} have different senses in the different ADAFs. The most important difference between the two models is that the dependence of ν_p on the magnetic field is much more sensitive in the resistive model. Therefore, the field strength is determined more accurately there. All the predicted dependences on m , \dot{m} , b_0 and δ are qualitatively confirmed in Figs. 2 through 5. From the above considerations on the synchrotron peak, we think that the improvement of observational quality in submillimeter range is most important for obtaining more exact values of the disk parameters.

4.3.3. Bremsstrahlung

We shall try here to grasp the qualitative behavior of the contribution from bremsstrahlung according to the usual non-relativistic scheme. The contribution to a given frequency ν from optically thin plasma in an annular volume of width dR is proportional to $\rho^2 T^{-1/2} \exp[-h\nu/k_B T] R^2 dR$. Apart from the exponential factor, we have

$$\begin{aligned} \rho^2 T^{-1/2} R^2 dR &\propto \alpha^{-2} \dot{m}^2 m r^{-1/2} dr \quad (\text{viscous ADAF}), \\ &\propto \delta^{-4} b_0^{-2/5} \dot{m}^{11/5} m^{4/5} r^{1/2} dr \\ &\quad (\text{resistive ADAF}). \end{aligned} \quad (43)$$

Therefore, the relative importance of the inner and outer parts of a disk can be seen from the ratio,

$$f \equiv \frac{\rho_{\text{in}}^2 T_{\text{in}}^{-1/2} R_{\text{in}}^2 \exp[-h\nu/k_{\text{B}}T_{\text{in}}]}{\rho_{\text{out}}^2 T_{\text{out}}^{-1/2} R_{\text{out}}^2 \exp[-h\nu/k_{\text{B}}T_{\text{out}}]} \simeq \zeta^{\pm 1/2} \exp[h\nu/k_{\text{B}}T_{\text{out}}], \quad (44)$$

where $\zeta \equiv R_{\text{out}}/R_{\text{in}} = r_{\text{in}}^{-1}$, and the upper and lower signs in its exponent are for the viscous and resistive ADAFs, respectively.

It is evident from the above ratio that, in the viscous ADAF, the contribution from the inner disk is always dominant (i.e., $f > 1$) irrespective of the frequency ν . In the resistive ADAF, however, it depends on the frequency, so that we introduce the critical frequency ν'_c by the relation $f = 1$. This yields

$$\nu'_c = \frac{\ln \zeta}{2} \frac{k_{\text{B}}T_{\text{out}}}{h}. \quad (45)$$

Then, the inner part contributes to the frequency range $\nu > \nu'_c$ and the outer part, to $\nu < \nu'_c$. In fact, the critical frequency roughly coincides with the peak frequency of the bremsstrahlung. The luminosity above ν'_c can be roughly estimated, by putting $dr \sim r \sim r_{\text{in}}$, as

$$\begin{aligned} L_{\nu}^{\text{br}} &\propto \alpha^{-2} \dot{m}^2 m && \text{(viscous ADAF),} \\ &\propto \delta^{-1} b_0^{-2/5} \dot{m}^{11/5} m^{4/5} && \text{(resistive ADAF),} \end{aligned} \quad (46)$$

because r_{in} is a numerical constant and, in particular, equal to δ^2 in the resistive ADAFs.

In the viscous ADAF models and in the compact-disk case of the resistive ADAF, the contributions from bremsstrahlung cause an X-ray bump in each predicted spectrum. The dependences of this peak on the parameters m and \dot{m} are qualitatively confirmed in Figs. 2 and 3, but those on b_0 and δ are somewhat different from the above prediction, indicating a limitation of such a crude estimate as the above. The critical frequencies calculated from the best fit values for the compact and extended disks are 1.4×10^{19} Hz and 1.8×10^{15} Hz, respectively. The former value is in good agreement with the peak of the reproduced spectrum. In the extended-disk case, the contribution from the bremsstrahlung is negligibly small because the density throughout the disk becomes too small, and the X-ray range of the spectrum is explained by the once-scattered Compton photons.

5. SUMMARY & DISCUSSION

To summarize the examinations in the previous section, both viscous and resistive ADAF models can explain the observed spectrum of Sgr A* equally well. In spite of large differences in the basic mechanisms working in both models, the calculated spectra are quite similar, except for the extended-disk case in the resistive model. This fact suggests that also the resistive ADAF model is quite powerful in explaining the behavior of other low luminosity AGNs (Narayan, Mahadevan & Quataert 1998). In addition to these analogous aspects, the resistive model seems to have a possibility to explain such an essentially different situation as appeared in the extended disk case. In any case, when the presence of an ordered magnetic field should be taken seriously in some AGNs or in some stellar-size black holes then the resistive ADAF model, whose predictions on the radiation spectra are examined in this paper, will serve the purpose.

One of the most remarkable features of the ADAF models is that the mass of the central black hole seems to be

determined only from the fitting to the self-absorbed part of the observed spectrum. In the case of Sgr A*, the resistive ADAF model (hereafter restricting to the case of compact disk) predicts the central mass of $3.9 \times 10^5 M_{\odot}$ while the viscous models predict $1.0 \times 10^6 M_{\odot}$ (Manmoto et al. 1997) and $2.5 \times 10^6 M_{\odot}$ (Narayan et al. 1998). The accuracy of the fittings for other disk parameters than the black hole mass will be greatly improved by the precise determination of the position and height of the synchrotron peak from observations.

The black hole mass predicted by the resistive ADAF model is evidently smaller compared with the predictions of the viscous ADAF models. The latter values are consistent with the dynamically reduced value of $2.5 \times 10^6 M_{\odot}$ (Haller et al. 1996; Eckart & Genzel 1997), which may be considered as an upper limit for the black hole mass. In the history of viscous ADAF models, the predicted black-hole mass was as small as $7 \times 10^5 M_{\odot}$ (Narayan et al. 1995). Afterwards, by the inclusion of compressive heating, it becomes consistent with the dynamical mass. Since this change is mainly due to the decrease in electron temperature (Narayan et al. 1998), the prediction of the resistive ADAF model may also be increased if the development of its two-temperature versions results in a lower electron temperature. As for the compressive heating, it is already included in the resistive model.

In spite of the resemblance in the predicted spectral shape, there are of course many differences in the predictions of the viscous and resistive models. The precise dependences on the relevant quantities of the luminosities of the self-absorbed part, the synchrotron peak and the X-ray bump are different. Especially, the dependence of the synchrotron peak-frequency on the strength of magnetic field is much stronger for the resistive model. The essential difference in the geometry of an accretion flow may be in the radius of the inner edge rather than in its vertical thickness. The prediction of the resistive ADAF model for the inner-edge radius of the disk around Sgr A* is $\sim 20R_{\text{ms}}$, instead of the radius of marginally stable circular orbit R_{ms} . Although this result justifies the neglect of the general relativistic effects in our treatment, various questions may be raised about the behavior of infalling plasmas. As for this point we only present an idea below from a viewpoint of global consistency, because its detailed analyses are beyond the scope of this paper.

Fig. 1 shows an overview of the flow and magnetic field configurations (see K00, for more details). The accretion flow would be decelerated near the inner edge by the presence of a strong poloidal magnetic field which is maintained by the sweeping effect of the flow. As a result, a certain fraction of the accreting plasma will be turned its direction to go along the poloidal field lines, although the remaining fraction may fall into the central black hole. If the poloidal current driven in the accretion disk can close its circuit successfully around distant regions and along the polar axis, a set of bipolar jets will be formed (Kaburaki & Itoh 1987). Even if the mechanism for formation of jet does not work well, the plasma within the inner edge is likely to extend to the polar regions.

The presence of the plasma within the inner edge of an accretion disk and near the polar axis can be a possible source of the excess above the self-absorbed slope in radio band of the observed spectrum. Very recent VLBI observations of Sgr A* (Krichbaum et al. 1998; Lo et al. 1998) report that its intrinsic sizes in the east-west direction at 215 GHz and 68GHz are about $20 R_{\text{G}}$ (with $M = 2.5 \times 10^6 M_{\odot}$). A half of this size (i.e., its radius)

is just comparable to the size of the inner edge $\sim 60R_G$ of our model fitting with $M = 4 \times 10^5 M_\odot$. However, the value of the black hole mass estimated from the spectral fitting may be increased if there is a possibility for Sgr A* to have a wind-type mass loss from the surfaces of its disk (such possibilities have been noted for various types of objects by, e.g., Blandford & Begelman 1999; Di Matteo et al. 1999; Quataert & Narayan 1999). In such a case, the VLBI component becomes smaller than the size of the inner edge.

From the standpoint of the resistive ADAF, therefore, the above observations should be interpreted as suggesting the presence of a compact structure which is comparable to or smaller than the inner-edge radius of the accretion

disk. In view of the vertical elongation of this component reported by Lo et al. (1998), this structure is very likely to be the root of a jet as suggested by them. This picture is very consistent with the view described above in relation to Fig. 1. In this case, however, the location of the self-absorbed slope in the $\nu\text{-}\nu L_\nu$ diagram should be slightly shifted towards the higher-frequency side so that the VLBI data points can be regarded as an excess from the disk's contribution.

One of the authors (M. K.) would like to thank Tadahiro Manmoto for many valuable comments on the viscous ADAF models. He is also grateful to Umin Lee for his suggestions on some numerical technics.

REFERENCES

- Abramowicz, M. A., Chen, X., Kato, S., Lasota, J. -P., & Regev, O. 1995, *ApJ*, 438, L37
- Bisnovatyi-Kogan, G. S., & Lovelace, R. V. E. 1997, *ApJ*, 486, L43
- Blandford, R. D., & Begelman, M. C. 1999, *MNRAS*, 303, L1
- Coppi, P. S., & Blandford, R. D. 1990, *MNRAS*, 245, 453
- Di Matteo, T., Fabian, A. C., Rees, M. J., Carilli, C. L., & Ivison, R. J. 1999, *MNRAS*, 305, 492
- Eckart, A., & Genzel, R. 1997, *MNRAS*, 284, 576
- Fabian, A. C., Blandford, R. D., Guilbert, P. W., Phinney, E. S., & Cuellar, L. 1986, *MNRAS*, 221, 931
- Frank, J., King, A., & Raine, D. 1992, *Accretion Power in Astrophysics* (Cambridge: Cambridge University Press)
- Haller, J. W., Rieke, M. J., Rieke, G. H., Tamblyn, P., Close, L., & Melia, F. 1996, *ApJ*, 456, 194
- Jones, F. C. 1968, *Phys. Rev.*, 167, 1159
- Kaburaki, O. 1999, in *Disk Instabilities in Close Binary Systems*, ed. S. Mineshige et al. (Tokyo: Universal Academy Press), 325 (K99)
- Kaburaki, O. 2000, *ApJ*, in press (astro-ph 9910252) (K00)
- Kaburaki, O., & Itoh, M. 1987, *A&A*, 172, 191
- Kato, S., Fukue, J., & Mineshige, S. 1998, *Black-hole Accretion Disks* (Kyoto: Kyoto University Press)
- Krichbaum, T. P., Graham, D. A., Witzel, A., Greve, A., Wink, J. E., Grewing, M., Colomer, F., de Vicente, P., Gómez-González, J., Baudry, A., & Zensus, J. A. 1998, *A&A*, 335, L106
- Lightman, A. P., & Zdziarski, A. A. 1987, *ApJ*, 319, 643
- Lo, K. Y., Shen, Z.-Q., Zhao, J.-H., & Ho, P. T. P. 1998, *ApJ*, 508, L61
- Mahadevan, R. 1997, *ApJ*, 477, 585
- Mahadevan, R. 1999, *MNRAS*, 304, 501
- Mahadevan, R., Narayan, R., & Krolik, J. 1997, *ApJ*, 486, 268
- Mahadevan, R., Narayan, R., & Yi, I. 1996, *ApJ*, 465, 327
- Manmoto, T., Mineshige, S., & Kusunose, M. 1997, *ApJ*, 489, 791
- Nakamura, K. E., Kusunose, M., Matsumoto, R., & Kato, S. 1997, *PASJ*, 49, 503
- Narayan, R., & Yi, I. 1994, *ApJ*, 428, L13
- Narayan, R., & Yi, I. 1995a, *ApJ*, 444, 231
- Narayan, R., & Yi, I. 1995b, *ApJ*, 452, 710
- Narayan, R., Mahadevan, R., & Quataert, E. 1998, in *Theory of Black Hole Accretion Disks*, ed. M. A. Abramowicz, G. Bjornsson, & J. E. Pringle (Cambridge: Cambridge University Press), 148 (astro-ph 9803141)
- Narayan, R., Yi, I., & Mahadevan, R. 1995, *Nature*, 374, 623
- Narayan, R., Mahadevan, R., Grindlay, J. E., Popham, P. G., & Gammie, C. 1998, *ApJ*, 492, 554
- Quataert, E., & Narayan, R. 1999, *ApJ*, 520, 298
- Rybicki, G. B., & Lightman, A. P. 1979, *Radiative Processes in Astrophysics* (New York: John Wiley & Sons)
- Yusef-Zadeh, F., Morris, M., & Chance, D. 1984, *Nature*, 310, 557

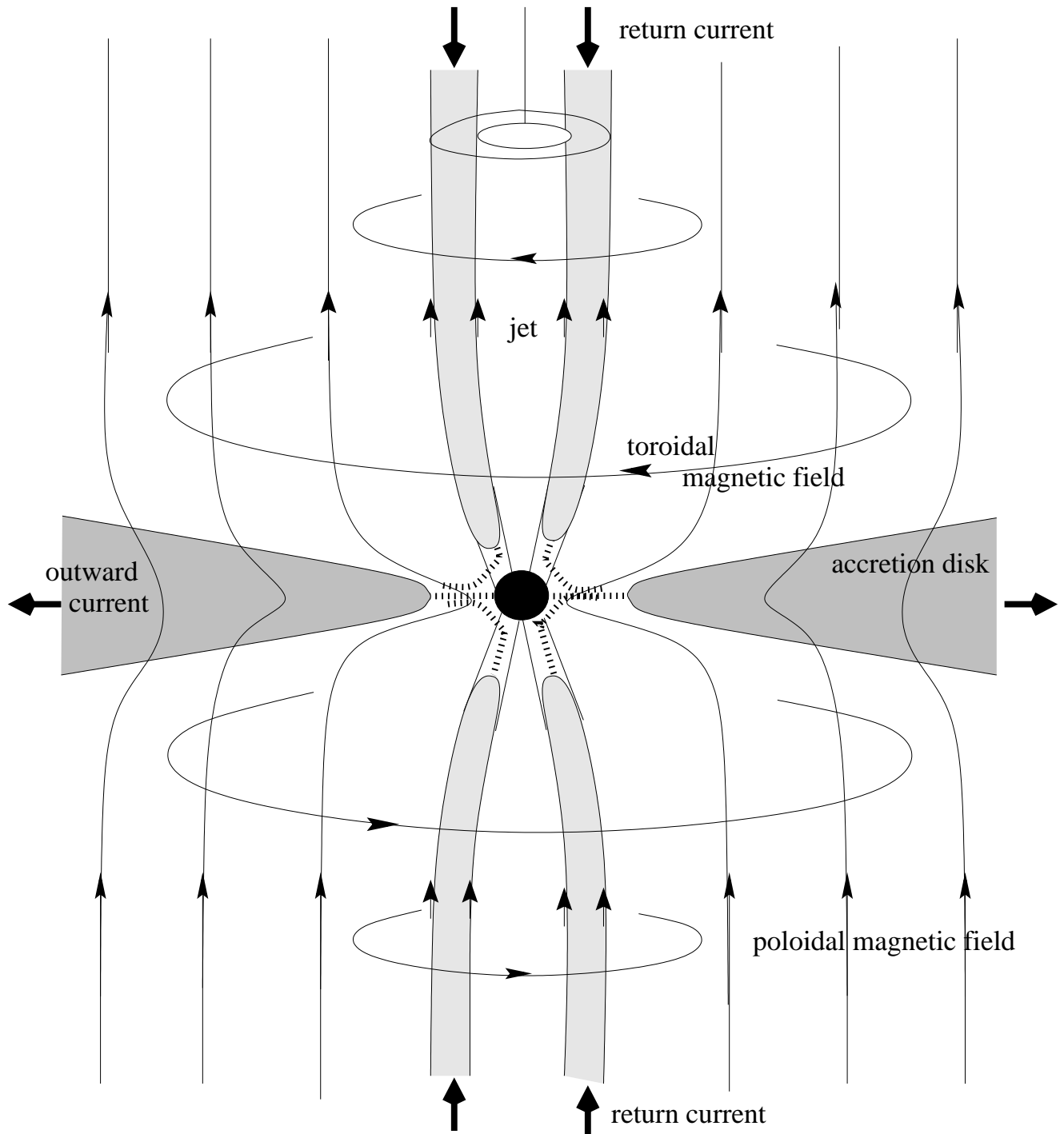


FIG. 1.— Schematic drawing of the global geometries of magnetic field and plasma flow. A poloidally circulating current system (j_p) driven by the rotational motion of accreting plasma generates a toroidal magnetic field b_φ in addition to a nearly uniform external field. The presence of this toroidal field outside the disk guarantees the magnetic extraction of angular momentum from the disk. This field also acts to confine the accreting flow toward the equatorial plane and has a tendency to collimate and accelerate the plasma in the polar regions. If the condition is favorable, the plasma in the polar regions may form a set of bipolar jets. In this paper, however, we focus our attention on the radiation spectrum from the accretion disk only.

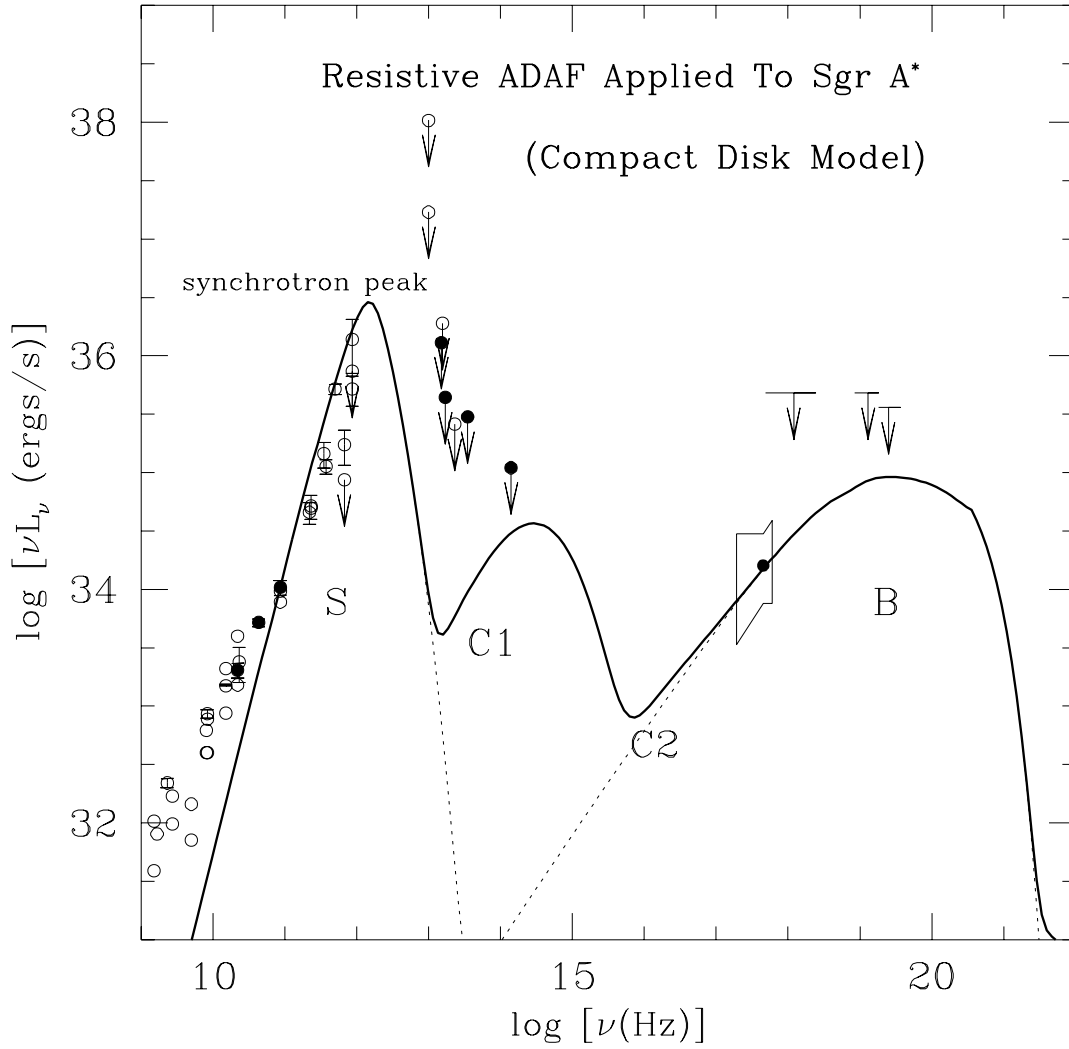


FIG. 2.— The best fit spectrum of Sgr A* in the compact disk model. The resulting physical quantities are $M = 3.9 \times 10^5 M_\odot$, $\dot{M} = 1.2 \times 10^{-4} \dot{M}_E$, $|B_0| = 0.7 \text{ G}$ and $\Delta = 0.14 \text{ rad}$. The four peaks indicated by S, C1, C2 and B denote those due to synchrotron emission, once- and twice-scattered (although it is almost buried) Compton photons and bremsstrahlung, respectively. The data points are the same as those compiled by Narayan et al. (1998).

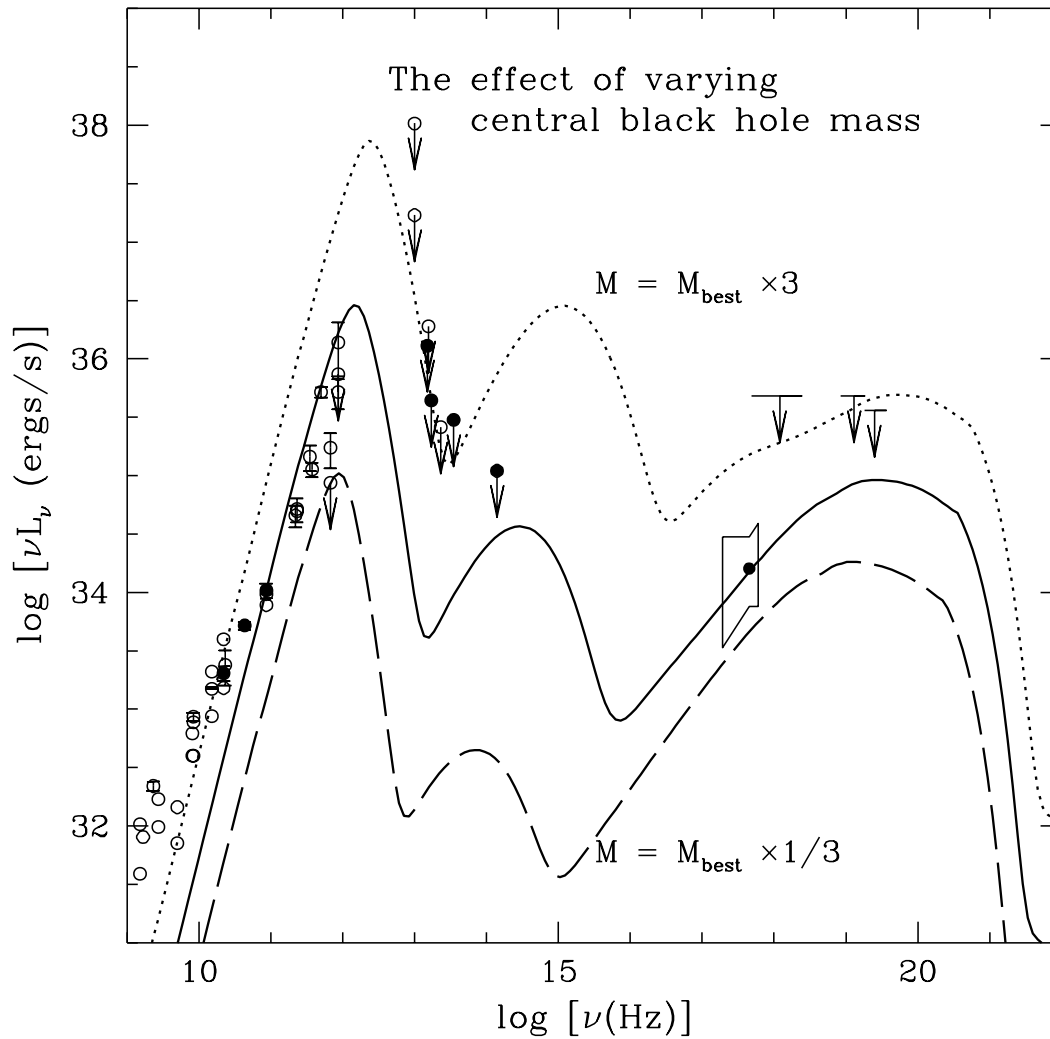


FIG. 3.— With increasing central mass, the luminosity νL_ν increases globally, so that the self-absorbed part shifts upward and the synchrotron peak-frequency shifts to higher frequencies. The direction of the shift of the synchrotron peak is different from the results of viscous ADAFs (Manmoto et al. 1997, Narayan et al. 1998).

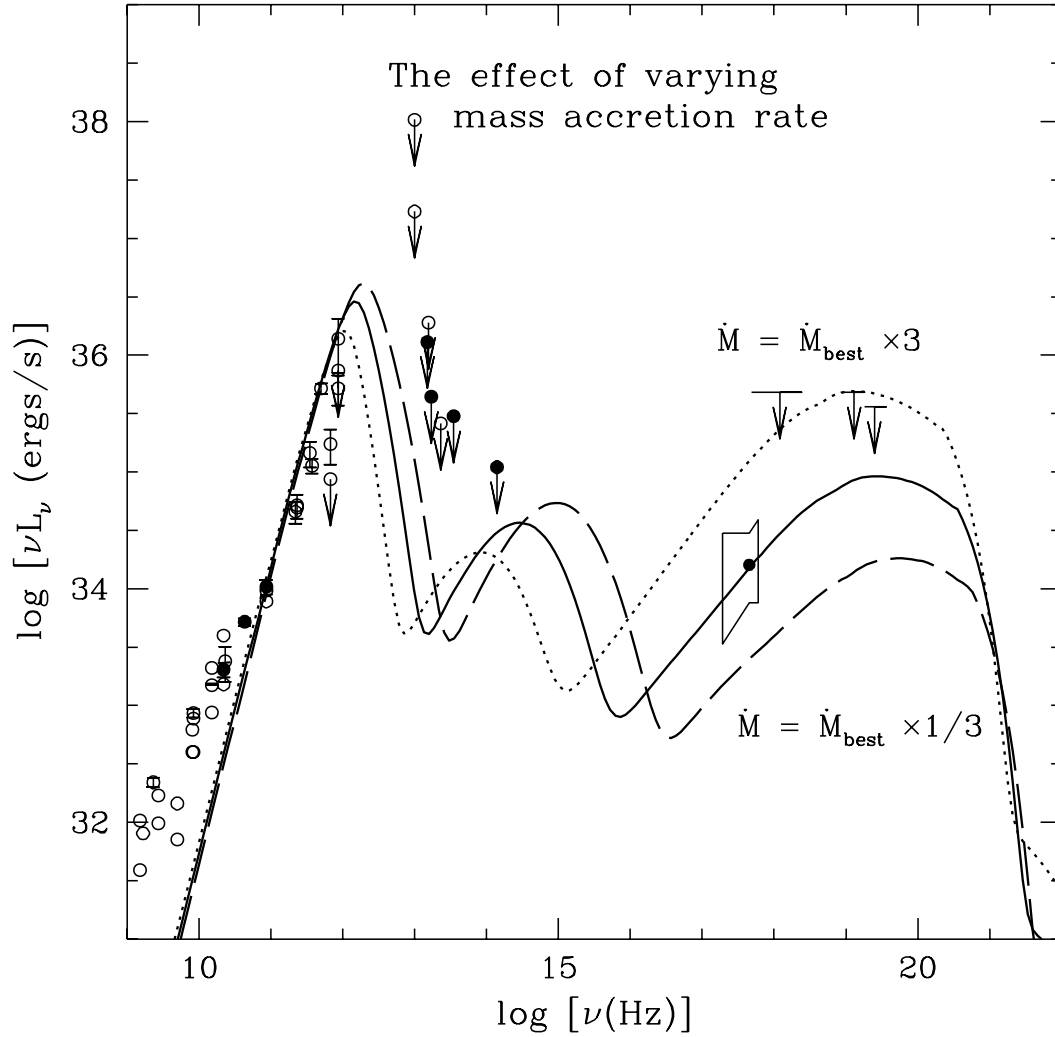


FIG. 4.— \dot{M} -dependence of the spectrum. With increasing mass accretion rate, the synchrotron peak shifts to lower frequencies while the self-absorbed luminosity is hardly affected. The former behavior is opposite to that of viscous ADAFs. The X-ray bump increases with \dot{M} .

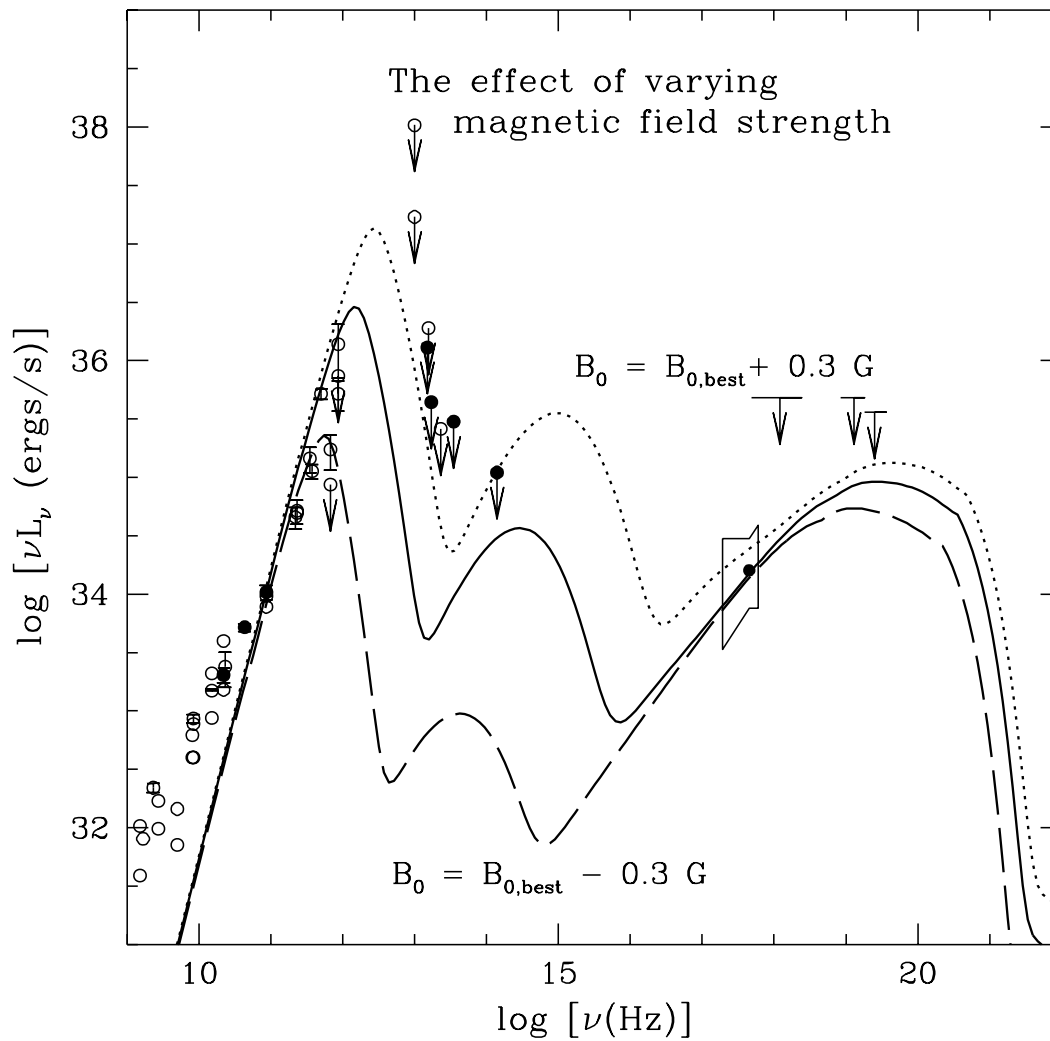


FIG. 5.— $|B_0|$ -dependence of the spectrum. With increasing magnetic field strength, the synchrotron peak shifts to higher frequencies while the self-absorbed luminosity is hardly affected. The X-ray bump increases with increasing $|B_0|$, suggesting a limitation of the crude estimate of L_ν^{br} given in the text.

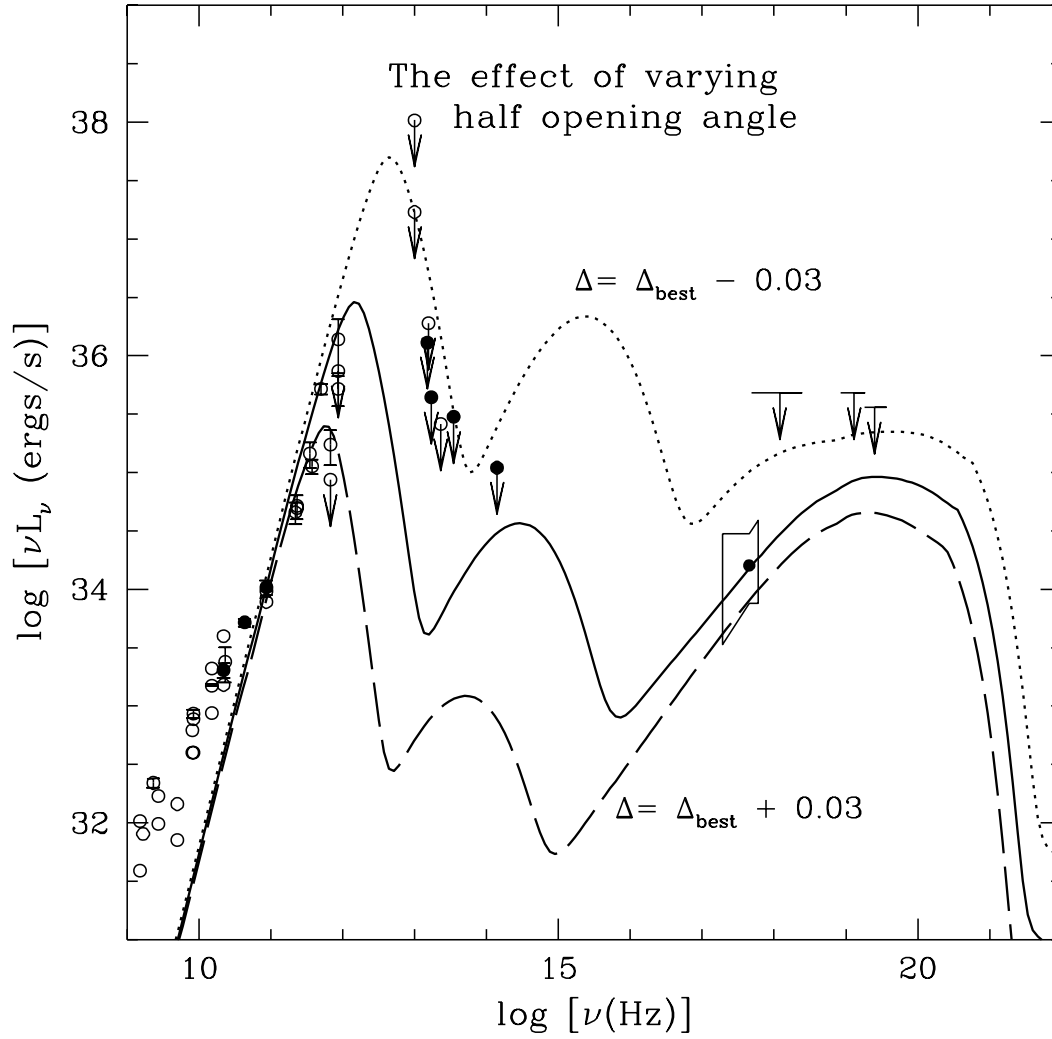


FIG. 6.— Δ -dependence of the spectrum. With increasing half-opening angle, the synchrotron peak shifts to lower frequencies while the self-absorbed luminosity is hardly affected. The dependence of the X-ray bump on Δ again suggests a limitation of the crude estimate given in the text.

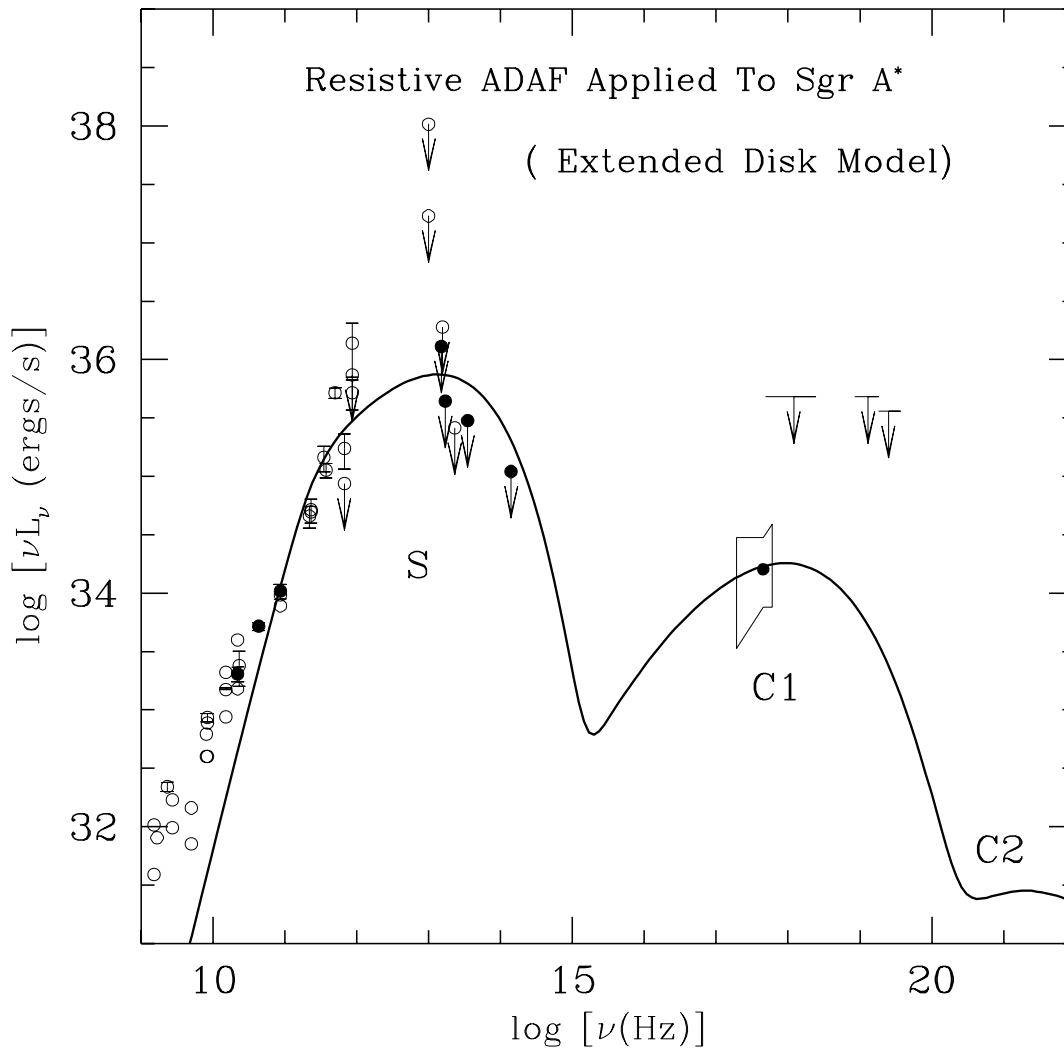


FIG. 7.— The best fit spectrum of Sgr A* in the extended disk model. The resulting physical quantities are $M = 1.0 \times 10^6 M_\odot$, $\dot{M} = 1.3 \times 10^{-4} \dot{M}_E$, $|B_0| = 1.0 \times 10^{-6} \text{ G}$, $\Delta = 0.20 \text{ rad}$. Among the four peaks which are seen in the case of compact disk, that of bremsstrahlung has disappeared owing to the low densities in the extended disk, so that the X-ray bump is explained by once-scattered Compton photons. The fitting both to 86 GHz and *ROSAT* X-ray data points is possible also in this model. However, the fitting in the frequency range from 100 to 1000 GHz becomes considerably poor compared with the case of compact disk, and it cannot be reconciled with the observed upper limits in the IR band. For these reasons, we judge that this model cannot reproduce the observed broadband spectrum of Sgr A*.

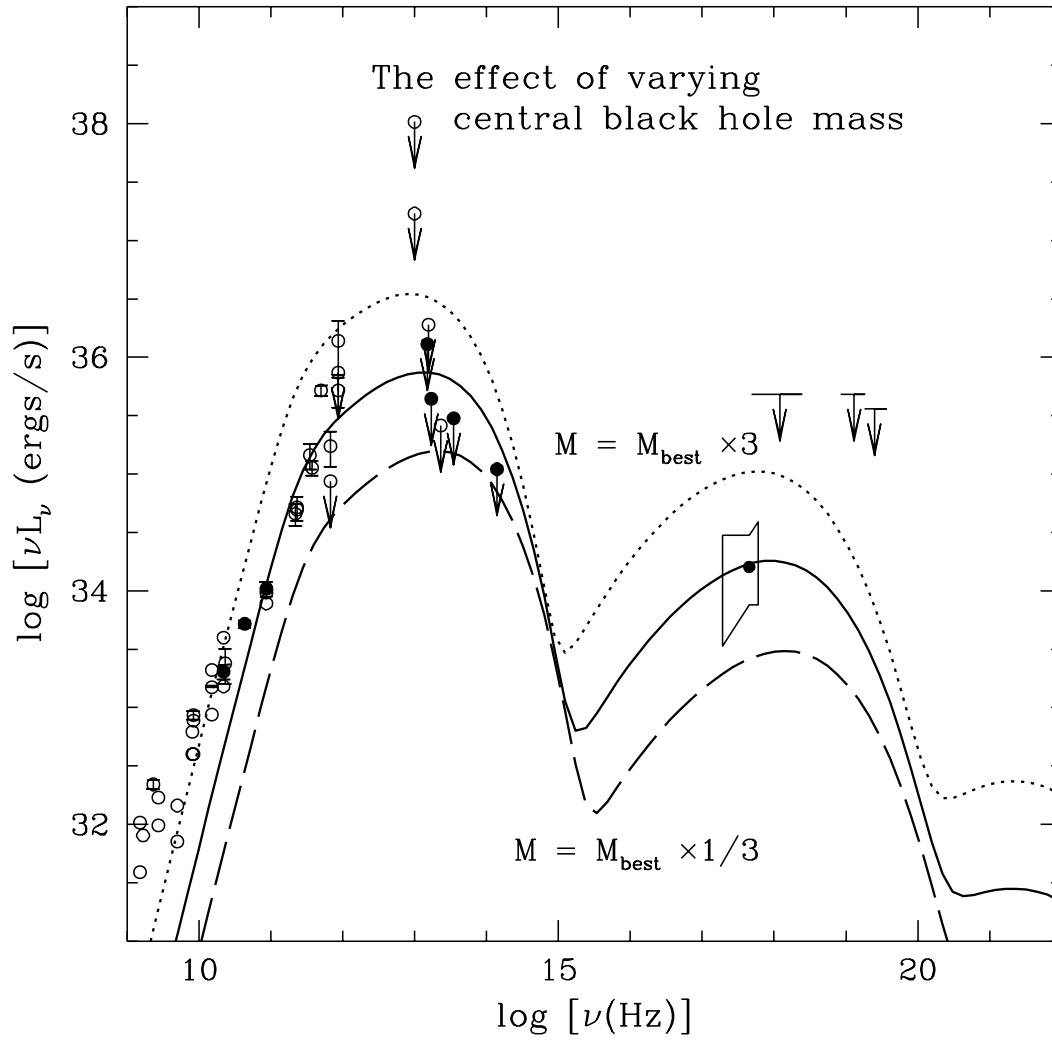


FIG. 8.— M -dependence of the spectrum. The tendency of the changes caused by varying M is almost the same as in the case of compact disk.

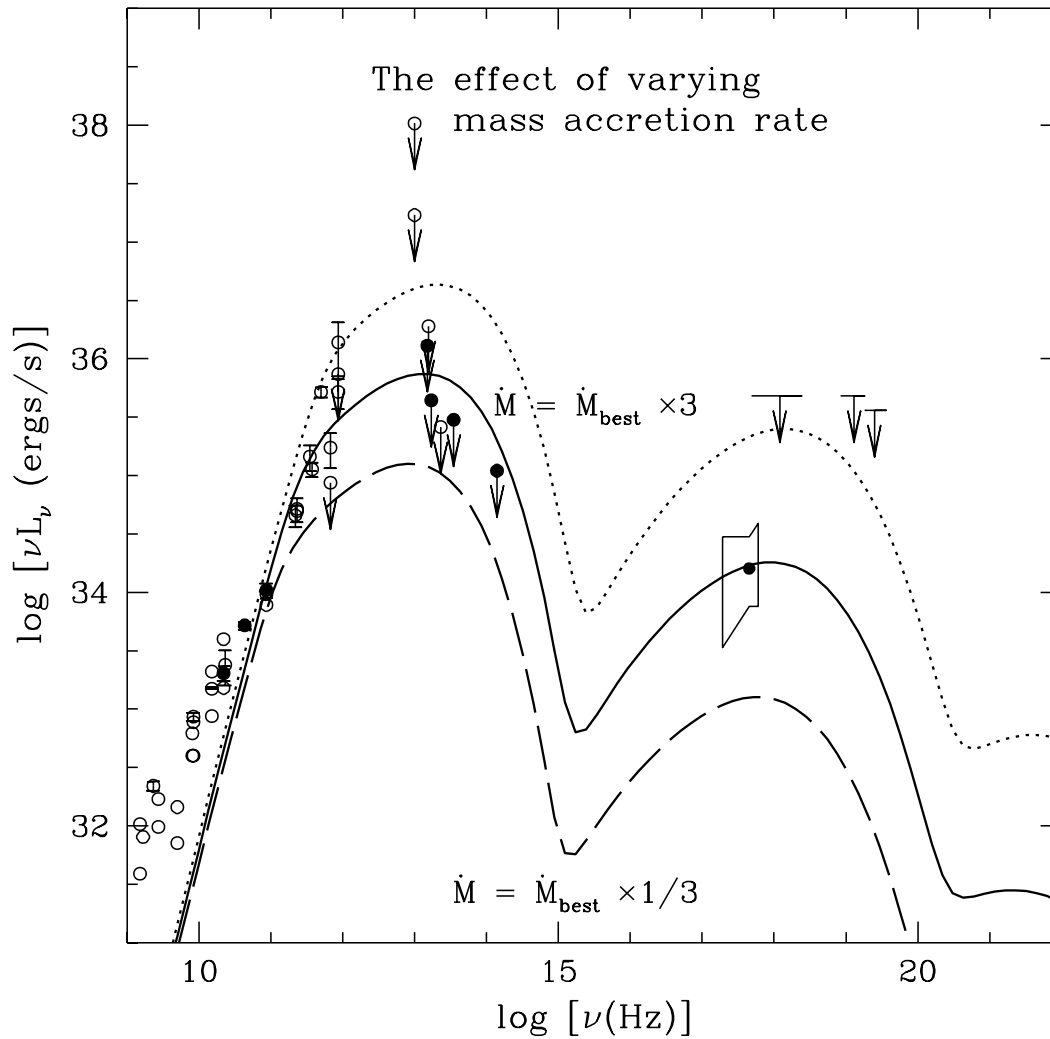


FIG. 9.— \dot{M} -dependence of the spectrum. With increasing mass accretion rate, the synchrotron peak shifts to higher frequencies while the self-absorbed luminosity is hardly affected. The former tendency is different from the case of compact disk.

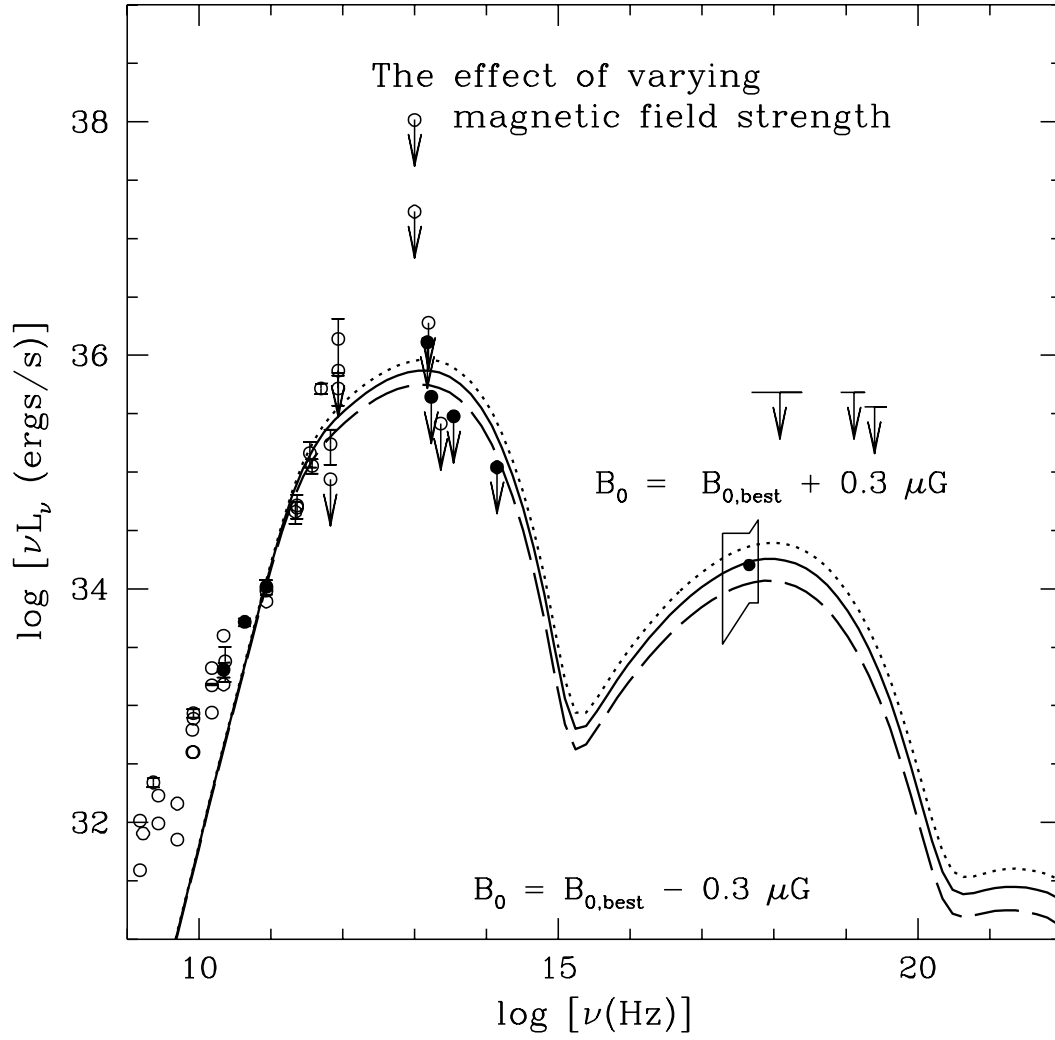


FIG. 10.— $|B_0|$ -dependence of the spectrum. The tendency is almost the same as in the case of compact disk.

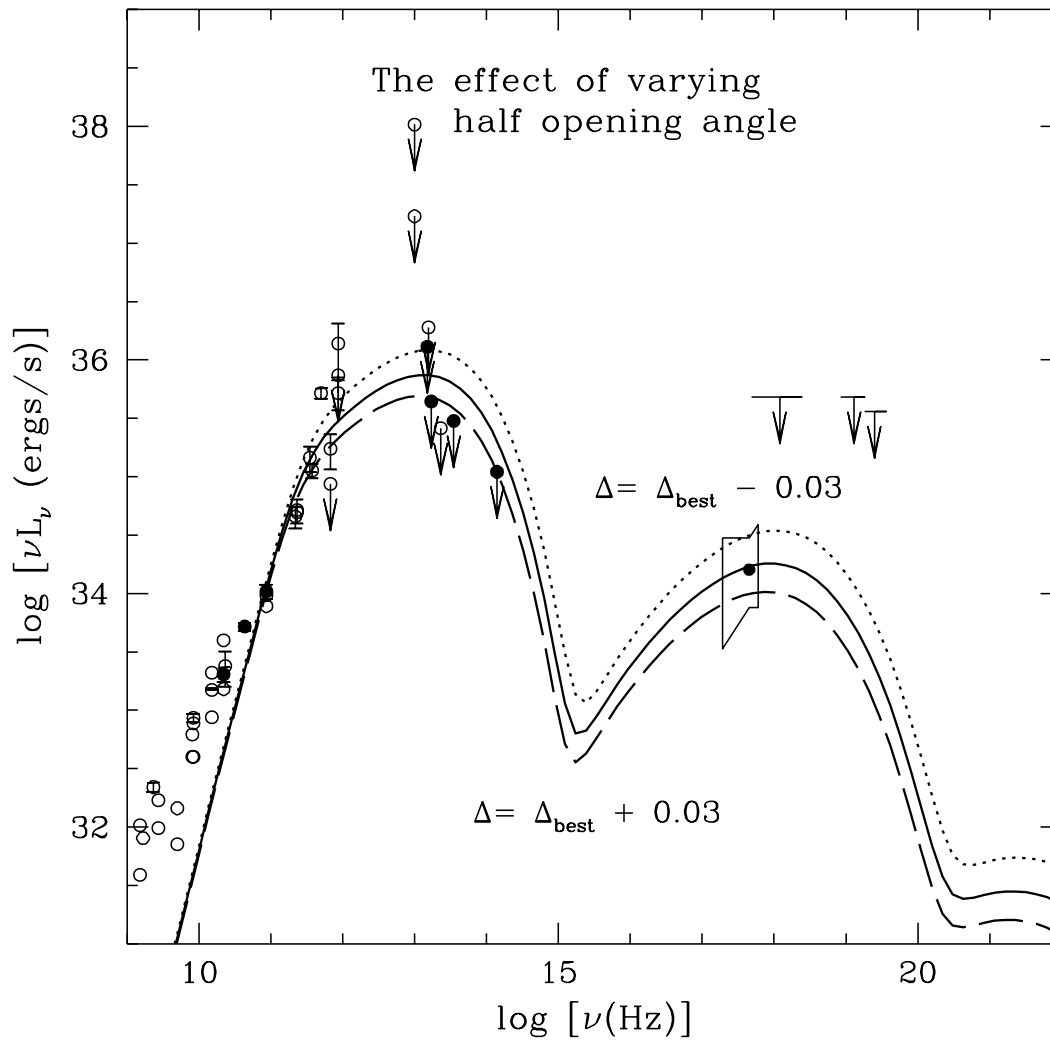


FIG. 11.— Δ -dependence of the spectrum. The tendency is almost the same as in the case of compact disk.